

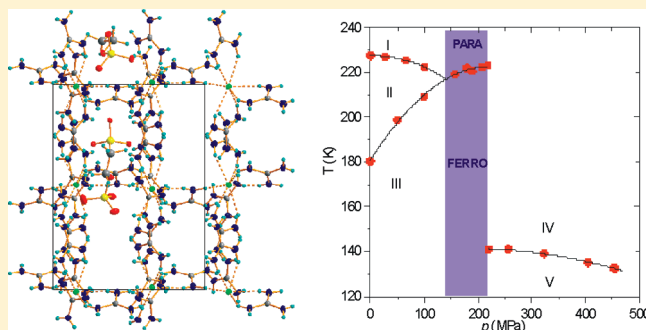
Crystal Structures, Phase Transitions, and Pressure-Induced Ferroelectricity in $[\text{C}(\text{NH}_2)_3]_5\text{SO}_4(\text{SO}_3-\text{OC}_2\text{H}_5)_2\text{F}$

Marek Szafranski*

Faculty of Physics, Adam Mickiewicz University, Umultowska 85, 61-614 Poznań, Poland

Supporting Information

ABSTRACT: A guanidinium compound, $[\text{C}(\text{NH}_2)_3]_5\text{SO}_4(\text{SO}_3-\text{OC}_2\text{H}_5)_2\text{F}$, with complex anionic sublattice has been synthesized and characterized by calorimetric and dielectric measurements at ambient and high hydrostatic pressures, as well as by single-crystal X-ray diffraction at varied temperatures. At room temperature, the crystal structure is orthorhombic, with the space group $Pnma$. In this phase, each of the two crystallographically nonequivalent ethoxysulfonate anions is disordered between two sites. On cooling, one of these anions starts to set in order at 228 K, where the crystal transforms in a continuous manner to the intermediate orthorhombic phase, with the space group $P2_12_12_1$. This transition belongs to the exceptionally rare pure gyrotropic phase transitions, the order parameter of which is described by the third-rank gyrotropic tensor. The ordering of the second ethoxysulfonate anion occurs suddenly at 187 K, inducing a first-order phase transition to the low-temperature phase of space group $Pna2_1$. The dissimilar response of both ethoxysulfonate anions to the temperature variation can be attributed to the different hydrogen bonding patterns they form with the cationic framework. Despite the polar symmetry, the low-temperature phase is not ferroelectric at ambient pressure, but it acquires ferroelectric features at elevated pressures above 140 MPa, as evidenced by the polarization reversal in an external electric field. The ferroelectric properties disappear on increasing pressure above 220 MPa, where the phase transition strongly modifying the crystal properties, but fully reversible, takes place. In the pressure-induced phase, a Debye-like dipolar relaxation process has been found and characterized as a function of pressure. The unusual properties of $[\text{C}(\text{NH}_2)_3]_5\text{SO}_4(\text{SO}_3-\text{OC}_2\text{H}_5)_2\text{F}$ under hydrostatic pressure have been summarized in the p – T phase diagram.



INTRODUCTION

Guanidine forms numerous complexes with mineral and organic acids. The planar conformation of the guanidinium cation, $[\text{C}(\text{NH}_2)_3]^+$, and its proneness to forming hydrogen bonds have been widely employed for the design and synthesis of new functional materials.^{1–6} For a long time, the interest in guanidinium salts has also been stimulated by the ferroelectricity of guanidinium sulfate hexahydrate, $\text{C}(\text{NH}_2)_3\text{Al}(\text{SO}_4)_2 \cdot 6\text{H}_2\text{O}$ (GASH), and several isomorphous compounds.^{7,8} Reports on the new ferroelectric guanidinium crystals^{9–12} have aroused a renewed interest in this subject. The search for new ferroelectric materials with superior properties is of great importance for developing modern electronic devices.^{13,14} Recently ferroelectric order has been found in the room-temperature phases of tetraguanidinium dichlorosulfate, $[\text{C}(\text{NH}_2)_3]_4\text{Cl}_2\text{SO}_4$,⁹ and tetraguanidinium dibromosulfate, $[\text{C}(\text{NH}_2)_3]_4\text{Br}_2\text{SO}_4$.¹⁰ Excellent ferroelectric properties have been observed at room temperature in supramolecular crystals of guanidinium perchlorate, $\text{C}(\text{NH}_2)_3\text{ClO}_4$, and guanidinium tetrafluoroborate, $\text{C}(\text{NH}_2)_3\text{BF}_4$.¹¹ The ferroelectric order is also realized in the low-temperature phase of guanidinium ethoxysulfonate,¹² $\text{C}(\text{NH}_2)_3\text{C}_2\text{H}_5\text{O}-\text{SO}_3$. The paraelectric phases of the $[\text{C}(\text{NH}_2)_3]_4\text{Cl}_2\text{SO}_4$ and $[\text{C}(\text{NH}_2)_3]_4\text{Br}_2\text{SO}_4$ crystals are isostructural (tetragonal space groups $I4_2m$),

but their room-temperature ferroelectric phases have different symmetries in space groups $Cmc2_1$ and $Fmm2$, respectively. Both compounds also exhibit promising piezoelectric activities. The spontaneous polarization, generated in their ferroelectric phases, originates from the ionic displacements occurring as a result of the crystal lattice response to the ordering of the SO_4^{2-} anions. The analysis of possible contributions to the total crystal polarization has shown a prominent role of the complex anionic sublattice in the mechanism of the electric dipole moments generation. The difference in the interplay of the monovalent Cl^-/Br^- and divalent SO_4^{2-} anions with the guanidinium cations leads to an asymmetry in the ionic arrangements, resulting in the sizable polarization. It appears that crystal structures built of mixed anionic (or cationic) sublattices may be of particular interest for the design and synthesis of new ferroelectric materials. On the basis of this strategy, in this study, a new complex guanidinium salt has been synthesized. The anionic framework of $[\text{C}(\text{NH}_2)_3]_5\text{SO}_4(\text{SO}_3-\text{OC}_2\text{H}_5)_2\text{F}$ is composed of monovalent F^- and $[\text{SO}_3-\text{OC}_2\text{H}_5]^-$ and of divalent SO_4^{2-} ions. The crystal structure

Received: May 16, 2011

Revised: July 14, 2011

Published: July 15, 2011

Table 1. Crystal Data and Structural Refinement Details for $[\text{C}(\text{NH}_2)_3]_5\text{SO}_4(\text{SO}_3-\text{OC}_2\text{H}_5)_2\text{F}$ at Ambient Pressure

	low-temp phase	intermediate phase	high-temp phase	
temp (K)	120	200	240	298
crystal system	orthorhombic	orthorhombic	orthorhombic	orthorhombic
space group	$Pna2_1$	$P2_12_12_1$	$Pnma$	$Pnma$
unit cell	a (Å)	20.353(4)	20.171(4)	20.272(5)
	b (Å)	14.179(3)	14.329(3)	10.583(3)
	c (Å)	10.415(3)	10.517(2)	14.348(3)
	V (Å ³)	3005.6(12)	3044.7(11)	3057.1(11)
Z , calcd density (g/cm ³)	4, 1.471	4, 1.452	4, 1.446	4, 1.439
θ range (deg)	2.43–26.06	2.02–26.06	2.02–26.06	2.01–25.07
refl collected/unique/ R_{int}	3120/3120/0.000	3258/3258/0.000	3175/3175/0.000	2869/2869/0.000
data/restraints/parameters	3120/1/521	3258/2/382	3175/22/253	2869/22/252
goodness-of-fit on F^2	1.048	1.036	0.991	1.094
indices R_1/wR_2 ($I > 2\sigma_I$)	0.0262/0.0661	0.0364/0.0933	0.0430/0.1160	0.0532/0.1603
R_1/wR_2 (all data)	0.0488/0.0721	0.0934/0.1094	0.1142/0.1378	0.1271/0.1865
largest peak and hole (e Å ^{−3})	0.244 and −0.243	0.426 and −0.291	0.393 and −0.440	0.432 and −0.377

and properties have been studied as a function of temperature and pressure. It has been demonstrated, among other things, that, at elevated pressures, the low-temperature phase of the crystal becomes a ferroelectric one.

The ferroelectric and ferroelectric-like materials have been the subject of intense pressure studies.^{15–20} However, among the numerous pressure-induced phenomena, the reports on ferroelectric phases, occurring exclusively under pressure, are relatively scarce. The well experimentally documented pressure-induced ferroelectricity has been reported, for example, for compounds $\text{Ca}_2\text{Ba}(\text{C}_2\text{H}_5\text{CO}_2)_6$,¹⁸ $[\text{N}(\text{CH}_3)]_2\text{FeCl}_4$,¹⁹ and $[\text{N}(\text{CH}_3)]_2\text{CuCl}_4$.²⁰

■ EXPERIMENTAL DETAILS

The compound $[\text{C}(\text{NH}_2)_3]_5\text{SO}_4(\text{SO}_3-\text{OC}_2\text{H}_5)_2\text{F}$ was synthesized by dissolving in water three simple guanidinium salts, $[\text{C}(\text{NH}_2)_3]_2\text{SO}_4$, $\text{C}(\text{NH}_2)_3\text{SO}_3-\text{OC}_2\text{H}_5$, and $\text{C}(\text{NH}_2)_3\text{F}$, in the molar ratio 1:2:1. Colorless, transparent single crystals were grown by evaporating the saturated solution at room temperature. The bulk crystals had linear dimensions 10–20 mm and were shaped as orthorhombic bipyramids.

At ambient pressure, the phase situation of the crystal was studied by differential scanning calorimetry (DSC). The measurements were carried out on a Q2000 calorimeter (TA Instruments). The DSC runs were recorded on heating and cooling the single-crystal sample at a rate of 10 K/min. Indium standard was used for temperature and enthalpy calibration, and synthetic sapphire was used for heat capacity calibration.

Dielectric measurements were performed on the oriented single-crystal plates at ambient pressure and at hydrostatic pressures up to 460 MPa. The large surfaces of the plates were covered with sputtered gold electrodes. Measurements of the relative complex electric permittivity $\varepsilon = \varepsilon' - i\varepsilon''$ were carried out in the frequency range from 1 kHz to 10 MHz with a Hewlett-Packard 4192A impedance analyzer. The amplitude of the ac measuring electric field was about 3 V/cm. The temperature of the samples was changed at a rate ranging from 0.3 to 1 K/min, depending on the temperature range of the experiment. For high-pressure dielectric studies, the samples were mounted in a beryllium–copper pressure cell. Helium was used as the medium to transmit pressure from a gas compressor U11

(Unipress) to the measuring cell. The pressure was calibrated by means of a manganin gauge with an accuracy ± 3 MPa, and the temperature was controlled inside the cell with a copper–constantan thermocouple.

The polarization–electric field (P – E) dielectric hysteresis loops were recorded at several fixed hydrostatic pressures and temperatures with a Diamant–Drenck–Pepinsky bridge method²¹ at a frequency of 50 Hz.

The single-crystal X-ray diffraction studies were carried out using a KM-4 diffractometer operating with graphite-monochromated Mo $K\alpha$ radiation. The data were collected at 120, 200, 240, and 300 K. The θ – 2θ scan mode at variable rate, depending on the reflection intensity, was applied. The intensities were corrected for Lorentz effect, polarization effect, and absorption. The unit-cell dimensions were measured as a function of temperature by least-squares fits to 32 automatically centered reflections. The crystal was cooled/heated with a nitrogen stream using an Oxford Cryosystem attachment. The temperature of the stream was stabilized within 0.1 K.

The crystal structures were solved by direct methods with the SHELXS97 program,²² and they were refined by full-matrix least-squares method on all intensity (F^2) data using the SHELXL97 program.²³ All the heavy atoms were refined with anisotropic temperature factors. At the early stage of the structure modeling at 120 K, the H atoms were placed in geometrically ideal positions after each cycle of the refinement, but in the final steps, they were refined without any constraints, with isotropic thermal parameters. For the structure determinations at higher temperatures, the H atoms were located from the molecular geometry and refined using a rigid group model. The isotropic temperature factors U_{iso} of the hydrogen atoms were assumed to be 1.2, 1.2, and 1.5 times the U_{eq} of their closest heavy atoms in NH_2 , CH_2 , and CH_3 , respectively. The crystal data, together with experimental and refinement details, are listed in Table 1. Full documentation has been deposited in the Cambridge Crystallographic Database Centre as supplementary publications CCDC 821052, CCDC 821053, CCDC 821054, and CCDC 821055 for the structures determined at 120, 200, 240, and 298 K, respectively. These data are also included as CIF files in the Supporting Information.

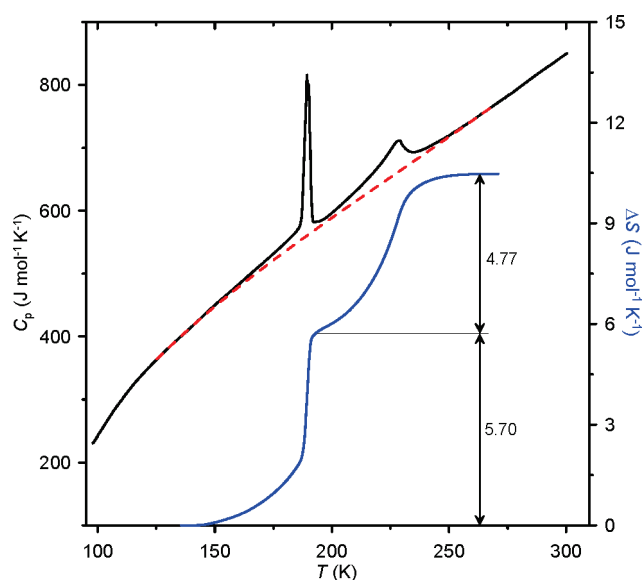


Figure 1. Specific heat and entropy changes in the vicinity of phase transitions in $[\text{C}(\text{NH}_2)_3]_5\text{SO}_4(\text{SO}_3-\text{OC}_2\text{H}_5)_2\text{F}$. The dashed line shows the baseline adopted for the integration of the anomalous parts of $C_p(T)$ and for ΔS calculations.

RESULTS AND DISCUSSION

Specific Heat Measurements. The temperature dependence of heat capacity $C_p(T)$, derived from the DSC heating run (Figure 1), indicates a sequence of two phase transitions in the crystal under study. The sharp peak at 187 K exhibits features characteristic of a first-order phase transition while the anomaly peaking at 228 K is typical of a second-order phase transition. Thus, at ambient pressure, $[\text{C}(\text{NH}_2)_3]_5\text{SO}_4(\text{SO}_3-\text{C}_2\text{H}_5\text{O})_2\text{F}$ has three crystalline phases. Hereafter, the high-temperature, intermediate, and low-temperature phases are denoted as I, II, and III, respectively. The lower curve in Figure 1 illustrates the entropy changes associated with both phase transitions. The anomalies in $C_p(T)$ were integrated in the assumption that the normal course of the crystal specific heat is approximated by a smooth baseline marked in the figure as the dashed line. The total entropy gain, related to the transitions, is close to $10.5 \text{ J mol}^{-1} \text{ K}^{-1}$. A precise determination of the individual transition entropies was hindered as a result of the partial overlapping of the thermal anomalies. The roughly estimated values $\Delta S_{32} = 5.70 \text{ J mol}^{-1} \text{ K}^{-1}$ for the first-order phase transition at $T_{32} = 187 \text{ K}$ and $\Delta S_{21} = 4.77 \text{ J mol}^{-1} \text{ K}^{-1}$ for the second-order phase transition at $T_{21} = 228 \text{ K}$ are both close to $R \ln 2$ (R is a gas constant). This indicates the configuration-type changes in the crystal structure at both phase transitions.

Temperature Dependence of Lattice Parameters. The unit cell dimensions of $[\text{C}(\text{NH}_2)_3]_5\text{SO}_4(\text{SO}_3-\text{OC}_2\text{H}_5)_2\text{F}$ were measured across the phase transitions region, in the temperature range 120–300 K. The results shown in Figure 2 confirm that the crystal undergoes two successive phase transitions. In the vicinity of T_{21} , the temperature changes in the lattice parameters and in the unit-cell volume proceed in a continuous manner, in accordance with a continuous character of the transition between phases I and II. As seen in Figure 2a, in phases II and III the lattice parameter a elongates with lowering temperature. The crystal elongation in this direction is also observed at the transition from the intermediate phase II to low-temperature phase III.

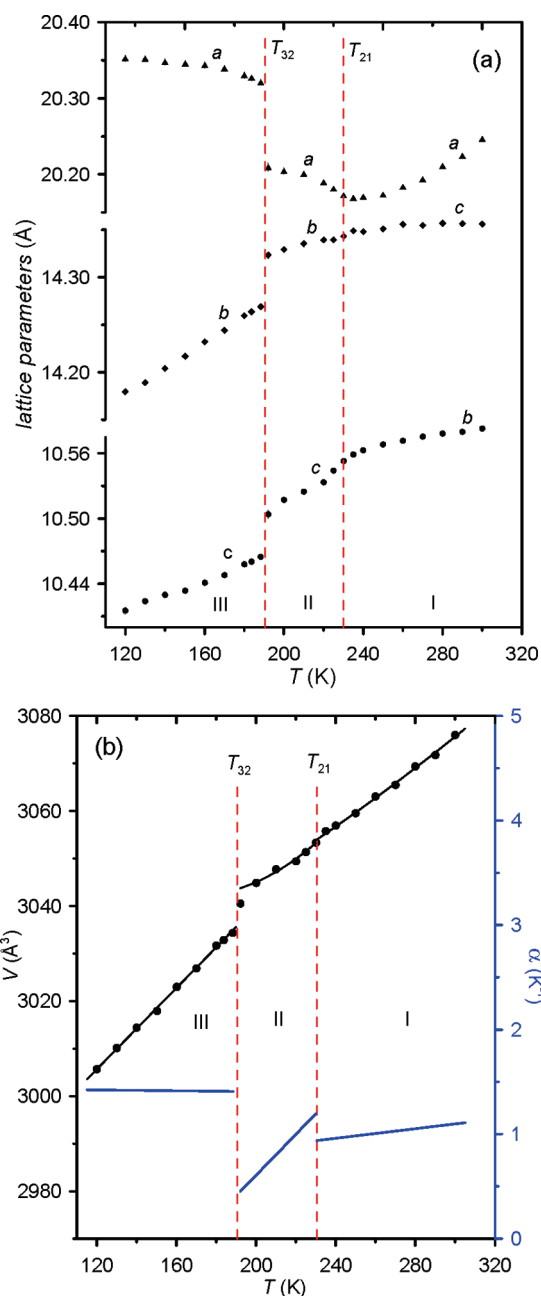


Figure 2. Temperature dependences of the lattice parameters (a) and unit-cell volume and volume thermal expansion (b) across the three ambient-pressure crystalline phases of $[\text{C}(\text{NH}_2)_3]_5\text{SO}_4(\text{SO}_3-\text{OC}_2\text{H}_5)_2\text{F}$. The standard deviations are marked by vertical bars, but mostly, they do not exceed the size of the symbols.

The anomalous thermal expansion along a is fully compensated by the normal temperature dependences of b and c , and hence, the unit-cell volume exhibits a typical temperature dependence—the crystal volume increases with increasing temperature. The stepwise character of the lattice parameters and the crystal volume change at T_{32} corroborate the first-order character of the transition between phases II and III. The temperature dependence of the unit-cell volume was described separately for each of the phases: by a linear function for phase III and by the second-order polynomial functions for phases II and I. The black solid lines in Figure 2b represent the best fits, which were used for the calculation of the

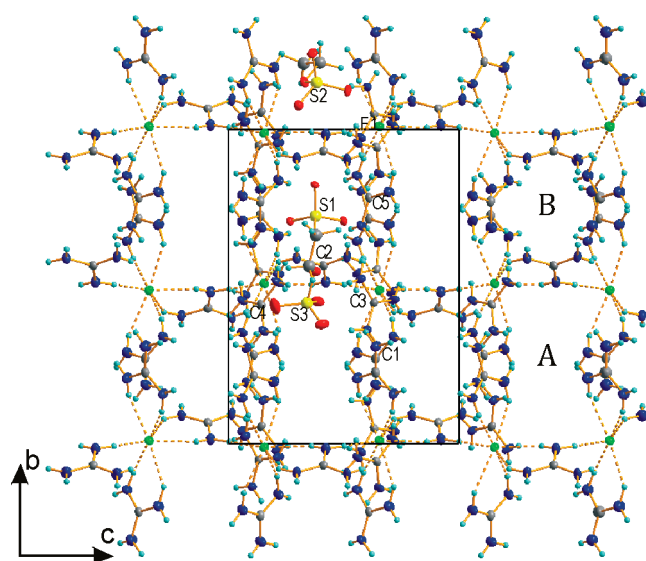


Figure 3. Crystal structure in phase III at 120 K projected on (100). To better illustrate the two symmetry independent channels A and B, running along [100], the ethoxysulfonate and sulfate anions are drawn only in the asymmetric part of the unit cell. Hydrogen bonds, represented by broken lines, are shown only between the guanidinium cations and the fluorine anions. Thermal ellipsoids of the heavy atoms are drawn at the 50% probability level.

volume thermal expansion coefficient, $\alpha = V^{-1} dV/dT$, plotted in Figure 2b. The extrapolation of the $V(T)$ dependences to T_{32} allowed us to derive the volume change at the first-order phase transition, $\Delta V = 8 \text{ \AA}^3$.

Crystal Structures Description. The X-ray diffraction data collected at various temperatures indicate that in the temperature range of both phase transitions the crystal remains in the orthorhombic system, changing its space group symmetry from $Pnma$ in phase I to $P2_12_12_1$ in phase II and next to $Pna2_1$ in phase III (see also Table 1). The noncentrosymmetric space groups of the two low-temperature phases are both the subgroups of the centrosymmetric space group of phase I, but there is not a group–subgroup relation between phases II and III. Thus, the symmetry changes permit a continuous phase transition between phases I and II and imply the first-order character of the transition between phases II and III, as it is observed actually. Most interesting, the transition $Pnma \rightarrow P2_12_12_1$ is a very rare example of a pure gyrotropic phase transition, which was observed for the first time in the bis(pentylammonium)tetrachlorozincate-(II) crystals.²⁴ For such a transition, the order parameter is a third-rank tensor, and hence, the transition can be characterized by optical activity and piezoelectric properties.

Figure 3 illustrates the crystal structure in phase III at 120 K projected on (100). For clarity of the picture, the SO_4^{2-} and $[\text{SO}_3-\text{OC}_2\text{H}_5]^-$ anions were drawn only for the asymmetric part of the unit cell. When the structure is viewed along [100], two different channels, marked in Figure 3 as A and B, can be distinguished. These channels are formed of guanidinium cations and fluorine anions tied to the cationic sublattice by the $\text{N}-\text{H} \cdots \text{F}$ hydrogen bonds. The SO_4^{2-} anions occupy sites in channel B; the ethoxysulfonate anions ES2 (the numbering of the sulfur atoms was adopted for the anions) are accommodated in channel A; and the ethoxysulfonate anions ES3 are located so that the SO_3 groups are placed in channel A, while the OC_2H_5

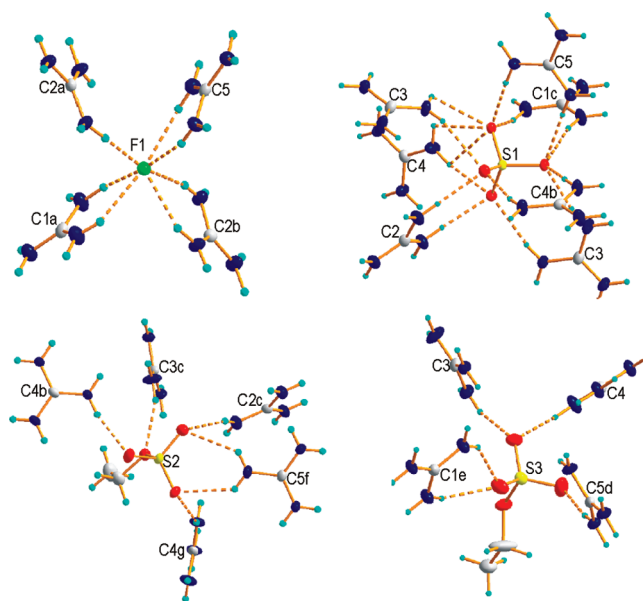


Figure 4. Hydrogen bonding of anions in phase III at 120 K. Thermal ellipsoids are drawn at the 50% probability level, hydrogen atoms are spheres with arbitrary radii, and hydrogen bonds are drawn as dashed lines. Symmetry codes: $a (-0.5 + x, 1.5 - y, z)$; $b (0.5 - x, 0.5 + y, 0.5 + z)$; $c (0.5 - x, 0.5 + y, -0.5 + z)$; $d (-x, 1 - y, -0.5 + z)$; $e (-0.5 + x, 0.5 - y, z)$; $f (-x, 2 - y, -0.5 + z)$; $g (x, 1 + y, z)$.

moieties penetrate into channel B. The sulfate and ethoxysulfonate ions are tied to the cationic framework by a complex network of $\text{N}-\text{H} \cdots \text{O}$ hydrogen bonds. The surroundings of the anions are shown in Figure 4.

The crystal structure is well ordered only in the low-temperature phase III. In the intermediate phase II, one of the two ethoxysulfonate anions, occupying different crystallographic sites, is disordered. The ethoxysulfonate anions and their hydrogen bonding, derived from the refinement of the crystal structure in phase II at 200 K, are shown in Figure 5. The occupancy factors of the split oxygen atoms O32A/O32B and O33A/O33B were initially refined, but as they deviated only slightly from the 50/50 occupancy, they were finally fixed with that ratio. The rest of the atoms of the anion ES3 were refined as ordered, but in fact, they can be disordered between the close sites, which is behind the resolution of the method. The two-site disorder is in excellent agreement with the transition entropy change of $R \ln 2$, measured for the phase transition at $T_{32} = 187 \text{ K}$. At 200 K the anion ES2 is not split, but the terminal carbon atom, C5, of the ethoxy group exhibits an enhanced ellipsoid of thermal vibrations, indicative of a possible onset of disorder. This suggestion is supported by the anomalous entropy change observed in phase II (see Figure 1). The structure refinements at 240 and 298 K showed that both ethoxysulfonate anions are disordered in phase I (see Figure 5). Thus, it is reasonable to assume that the disorder of the anion ES2 starts just above T_{32} and continuously grows with increasing temperature up to the transition point at $T_{21} = 228 \text{ K}$, where the symmetry breaking takes place. In phase I, the disorder of the anions is such that the arrangement of partially occupied sites fulfills the symmetry of a mirror plane perpendicular to [010].

The activation of the anionic disorder in different temperature ranges can be rationalized by considering the surroundings of the ions and, in particular, the differences in the hydrogen bonding. As shown in Figure 4, the anion ES3 is tied to the guanidinium

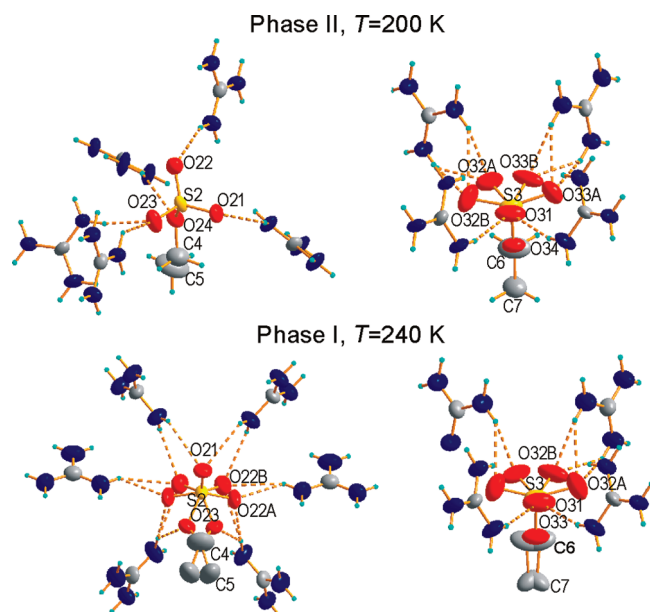


Figure 5. Two symmetry independent ethoxysulfonate anions in phase II at 200 K and in phase I at 240 K. For disordered groups, the hydrogen atoms are omitted. Thermal ellipsoids are drawn at the 50% probability level, and hydrogen bonds are drawn as dashed lines.

cations by five N–H···O hydrogen bonds, but only three oxygen atoms of the SO₄ group participate in the bonding. In the case of the anion ES2, all the oxygen atoms are involved in the H bonds. Thus, the anion ES2 is more strongly tied by hydrogen bonds to the cationic framework than ES3, and therefore, higher energy is required for the activation of its jumping.

Dielectric Properties at Ambient Pressure. The temperature dependence of the complex electric permittivity $\epsilon(\omega) = \epsilon'(\omega) - i\epsilon''(\omega)$ was measured for the electric field vector parallel and perpendicular to the crystallographic direction [001] of the low-temperature phase III (the c_{III} axis in phase III corresponds to the b_1 axis in phase I; see also Table 1 and Figure 2). At ambient pressure, the frequency dispersion of electric permittivity was small, and therefore, only the 200 kHz data are plotted in Figure 6. The dielectric response of the crystal is apparently anisotropic. Generally, in the whole temperature range, the magnitude of ϵ' is much higher along c_{III} than in the perpendicular direction. However, the most striking is the anomaly related to the continuous phase transition at T_{12} . In the direction perpendicular to c_{III} , this anomaly is hardly visible as a tiny change of the slope of the $\epsilon'(T)$ course, while along c_{III} it manifests as a well pronounced peak. At first glance, this peak resembles the anomalies observed at the paraelectric-to-ferroelectric phase transitions, but closer analysis indicates that this is not the case. The low-frequency dielectric constant does not obey the Curie–Weiss law, which is usually fulfilled in paraelectric phases of ferroelectric materials. Moreover, the symmetry considerations indicate that spontaneous polarization can occur only in the low-temperature phase III, where the crystal assumes the symmetry of the polar space group $Pna2_1$. Therefore, a ferroelectric phase transition could be expected at T_{23} rather than at T_{21} . On the other hand, the small stepwise dielectric anomaly observed at T_{23} (Figure 6) does not support this suggestion. A direct proof of ferroelectricity is a polarization reversal in an external electric field. A careful examination of the crystal showed that no trace of the P – E hysteresis loop was

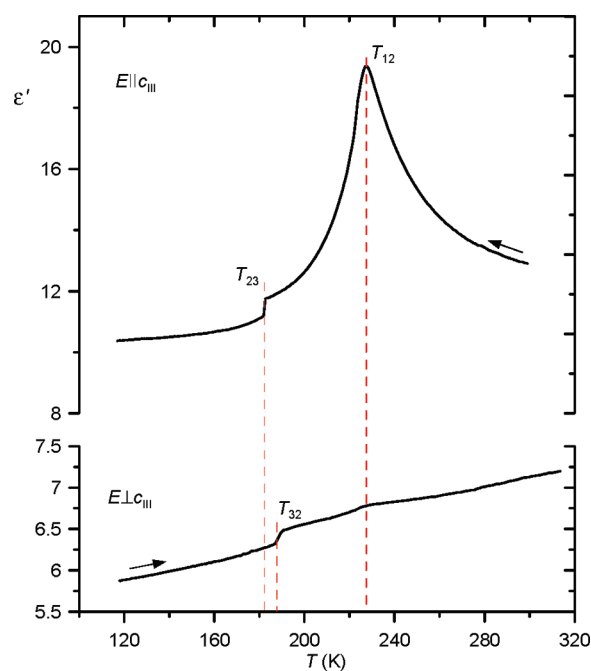


Figure 6. Temperature dependence of the dielectric constant of $[\text{C}(\text{NH}_2)_3]_5\text{SO}_4(\text{SO}_3-\text{OC}_2\text{H}_5)_2\text{F}$ measured at 200 kHz for electric field parallel (top) and perpendicular (bottom) to the crystallographic axis c_{III} ($c_{\text{III}} = c_{\text{II}} = b_1$).

observed either in phase II or in phase III. Although the ferroelectric order is not realized in $[\text{C}(\text{NH}_2)_3]_5\text{SO}_4(\text{SO}_3-\text{C}_2\text{H}_5\text{O})_2\text{F}$ at ambient pressure, the dielectric response of the crystal testifies to an extra contribution to the dielectric polarization. This contribution can arise from dipolar correlations of the OC₂H₅ moieties, jumping between different sites in the crystal lattice. The dipolar interactions are probably too weak to permeate a macroscopic volume of the crystal, but the resulting dipolar fluctuations give rise to the electric permittivity, especially in the vicinity of the continuous phase transition between phases I and II, where the critical fluctuations are expected. The symmetry breaking at T_{12} is induced by the ordering of one of the two different ethoxysulfonate anions, and therefore, the order parameter for the phase transition between phases I and II should be related to this process. The contribution of the critical fluctuations is also mirrored in the temperature dependence of the heat capacity. The long tail in the $C_p(T)$ anomaly, stretching over 25 K above T_{12} , in the high-temperature phase (see Figure 1), most probably results from such fluctuations.

Pressure-Induced Effects. The untypical dielectric response of $[\text{C}(\text{NH}_2)_3]_5\text{SO}_4(\text{SO}_3-\text{OC}_2\text{H}_5)_2\text{F}$ suggests that, at varied thermodynamic conditions, the crystal can acquire new properties. Among the thermodynamic parameters, pressure is one of these, which can change intermolecular distances and thus modify the dipole–dipole interplay. The hydrostatic pressure was applied at room temperature, and next, the electric permittivity was measured on cooling and on heating the sample through the phase transitions region. The results of these measurements are summarized in the form of the p – T phase diagram in Figure 7. For this purpose, the transition temperatures were taken from the cooling runs. The application of a relatively low pressure results in spectacular changes of the crystal dielectric properties. As shown in Figure 8, the anomaly associated with the continuous

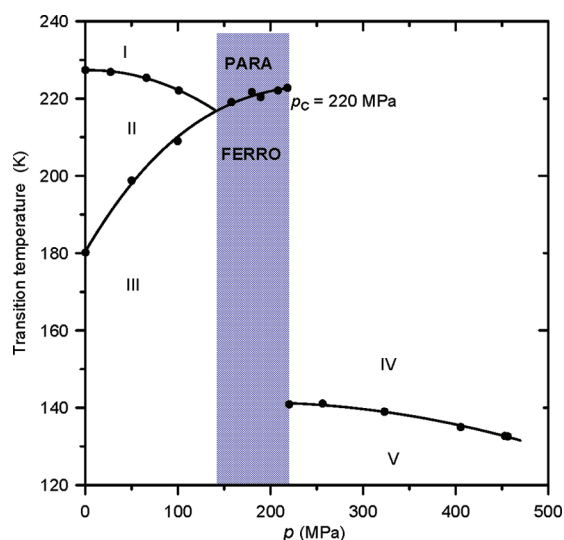


Figure 7. p – T phase diagram of $[\text{C}(\text{NH}_2)_3]_5\text{SO}_4(\text{SO}_3\text{--OC}_2\text{H}_5)_2\text{F}$. The shaded region marks the pressure range where the crystal acquires ferroelectric properties.

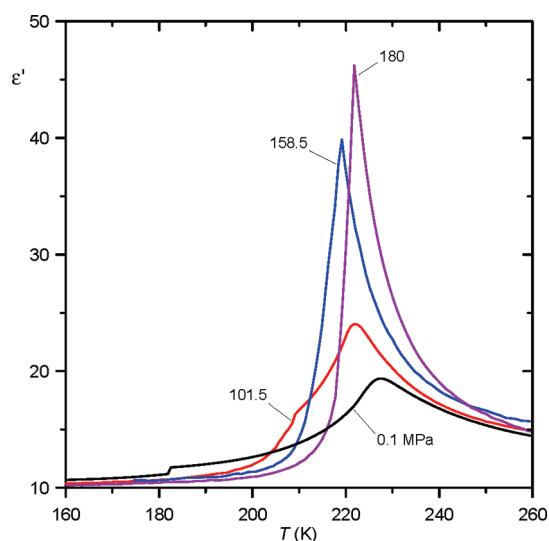


Figure 8. Pressure-induced changes in the dielectric constant of $[\text{C}(\text{NH}_2)_3]_5\text{SO}_4(\text{SO}_3\text{--OC}_2\text{H}_5)_2\text{F}$ measured as a function of temperature. The 200 kHz electric field was applied along the c_{III} axis.

phase transition at T_{12} grows profoundly at elevated pressures. In the pressure range up to 140 MPa, the transition temperature T_{12} decreases with increasing pressure, but because of a reverse temperature dependence of T_{23} , the I/II and II/III phase boundaries meet at the multicritical point situated on the p – T plane at (140 MPa, 217 K). Under higher pressures, 140–220 MPa, only a single dielectric anomaly corresponding to the transition between the phases I and III was observed. In this pressure range, the dielectric anomaly is much more sharply shaped when compared to the rounded peak in the low-pressure range. This indicates that the transitions occurring below and above the multicritical point differentiate in nature. The transition between phases I and II is of second-order, while that between phases I and III shows the features characteristic for the first-order phase transitions. The first-order character of the I/III transition is evidenced by the

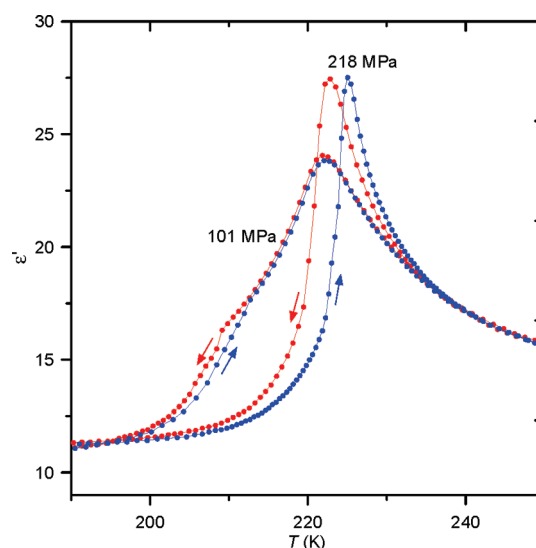


Figure 9. Dielectric anomalies measured on cooling and on heating [$E \parallel c_{\text{III}}$, $f = 250$ kHz] below the multicritical point at 101 MPa and above the multicritical point at 218 MPa.

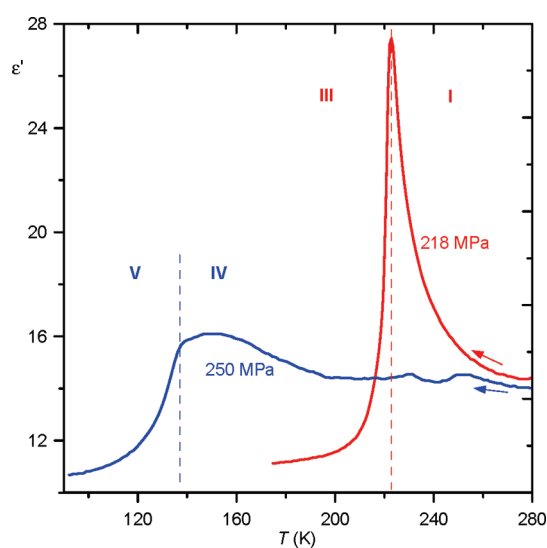


Figure 10. Comparison of the crystal dielectric response at 218 and 250 MPa ($f = 250$ kHz).

temperature hysteresis between the heating and cooling runs of $\epsilon'(T)$, as it is shown in Figure 9. The hysteresis raised, and the transition temperature shifted upward with increasing pressure. Above ca. 180 MPa, the peak amplitude started to diminish and suddenly disappeared under pressure exceeding 220 MPa, as illustrated in Figure 10. The profound change in the dielectric response of the crystal indicates the occurrence of a new polymorphic form, denoted hereafter as phase IV (see Figures 7 and 10). The substantial modification of the crystal properties strongly suggests a reconstructive nature of this transformation. Two small anomalies visible around 240 K on the 250 MPa scan, shown in Figure 10, can be ascribed to the regions where the transformation is incomplete. In the subsequent temperature runs, these anomalies decreased and finally disappeared. Such behavior was observed for all the studied samples but with different magnitudes of the effect. The presence of residual domains in the high-pressure

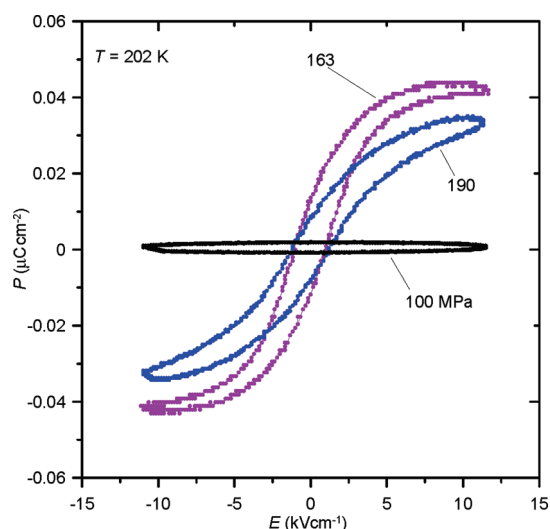


Figure 11. 50 Hz hysteresis loops of electric polarization recorded in phase III at 202 K for different hydrostatic pressures. The electric field was applied along the polar c_{III} axis.

phase IV testifies a reconstructive character of the pressure-induced structural transformations.

When phase IV is induced at room temperature and cooled, it passes in a continuous manner into phase V around $T_{45} = 140$ K. The transition temperature T_{45} decreases slightly with rising pressure. Noteworthy is a fully reversible character of the pressure-induced changes in the crystal structure. It was observed that the crystal came back to phase I when the pressure was released slowly below 220 MPa at room temperature. The occurrence of the initial phase I was testified by the presence of the sharp dielectric anomaly characteristic of the transition between phases I and III.

The strong enhancement of the dielectric response in the pressure range 0.1–180 MPa strongly suggests a possible pressure-induced ferroelectric order in the low-temperature phase III. To verify this hypothesis, the measurements of the P – E hysteresis loop were performed along the $[001]$ direction in this phase. The exemplary loops recorded at 202 K under pressures of 100, 163, and 190 MPa are shown in Figure 11. These measurements prove that spontaneous polarization, switchable in an external electric field, occurs in the crystal phase III, but only in the narrow pressure range 140–220 MPa. Thus, the transition temperature T_{13} is the Curie point, where the paraelectric-to-ferroelectric phase transition takes place. This is consistent with the symmetry change from the nonpolar space group $Pnma$ to the polar space group $Pna2_1$. Such a symmetry change allows the transition to be a continuous one, but the presence of temperature hysteresis (Figure 9) clearly indicates that, actually, this is not the case. The maximum spontaneous polarization P_s observed near 160–170 MPa well corresponds to the maximum amplitude of the dielectric anomaly in the same pressure range. Compared with previously reported ferroelectric guanidinium ethoxysulfonate,¹¹ the value of $P_s = 0.044 \mu\text{C cm}^{-2}$ determined at 163 MPa (see Figure 11) is lower by more than 1 order of magnitude. On the other hand, all the 50 Hz hysteresis loops recorded were relatively slim and displayed a low coercive field. The coercive field, estimated at the temperature 20 K below the Curie point, amounts to 1.2 kV cm^{-1} , that is comparable with GASH⁷ but much lower than in the recently discovered ferroelectric guanidinium complexes.^{9–11}

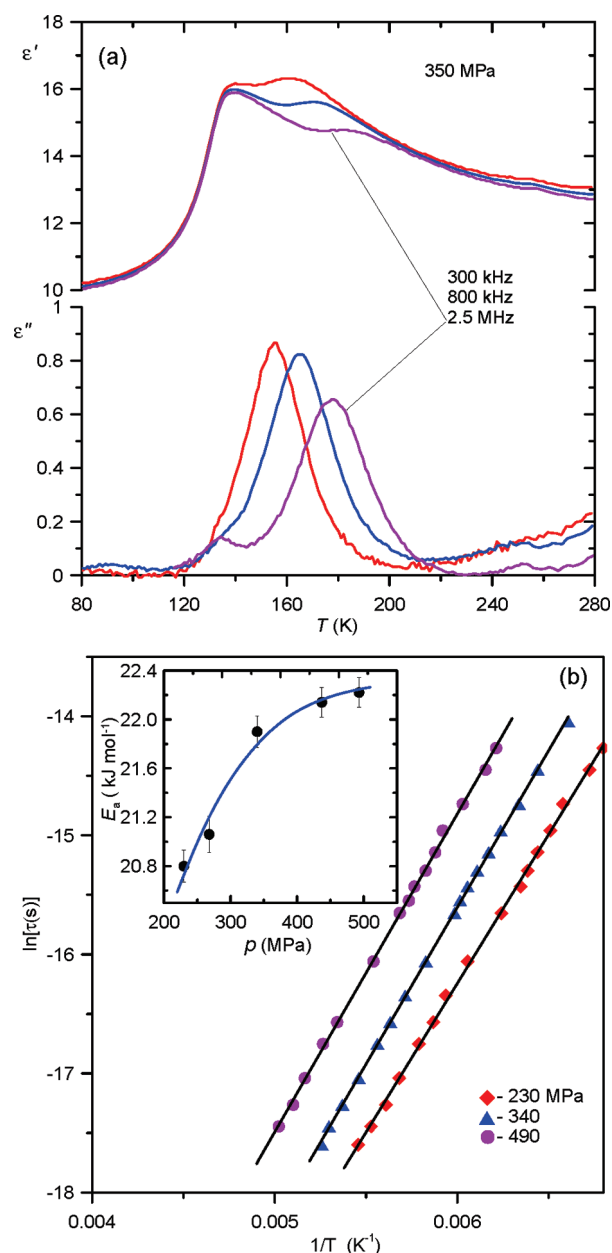


Figure 12. Frequency dispersion of the real (top) and imaginary (bottom) parts of the complex electric permittivity at 350 MPa (a) and Arrhenius plots, $\ln \tau$ vs reciprocal temperature, at 230, 340, and 490 MPa (b). The pressure dependence of the activation energy of the Debye-type relaxation process observed in the pressure-induced phase IV is shown in the inset in panel b. Black solid lines in panel b correspond to the best fits of the Arrhenius equation.

The dielectric response of the crystal in the pressure-induced phase IV exhibits a distinguishable frequency dispersion in the temperature range ca. 140–200 K, as illustrated in Figure 12a. This dispersion can arise from the slowing down of the ethoxysulfonate anions jumping between different sites in the crystal lattice, as a result of the temperature lowering. Thus, after the pressure-induced structure reconstruction, the crystal remains disordered down to the much lower temperatures than it does at ambient pressure. The Cole–Cole diagrams, that is, the $\epsilon''(\epsilon')$ dependencies, form semicircles, indicating a single Debye-type relaxation process. Accordingly, the relaxation time τ of the

dipolar motion was determined from the maxima of the $\varepsilon''(T)$ peaks, where the relation $\omega\tau = 1$ ($\omega = 2\pi f$ is the angular frequency of the applied ac electric field) is fulfilled. The temperature dependencies of the relaxation time at 230, 340, and 490 MPa are plotted in Figure 12b. The solid lines represent the best fits to the Arrhenius equation: $\tau = \tau_0 \exp(E_a/k_B T)$, where E_a is the activation energy of the dipolar relaxation and the pre-exponential, τ_0 , is a reciprocal of the attempt jump frequency. The activation energy, plotted as a function of pressure in the inset in Figure 12b, increases with increasing pressure, but this dependence is apparently nonlinear with a tendency to saturation at higher pressures above 400 MPa.

As shown in Figure 7, the boundary between phases III and II is nonlinear. The initial slope of this line, extrapolated to ambient pressure, $dT_{32}/dp = 0.38 \text{ K MPa}^{-1}$. This pressure coefficient can be determined independently from the Clausius–Clapeyron equation, $dT/dp = \Delta V/\Delta S$, where ΔV and ΔS are the volume and entropy changes at the transition temperature. The entropy change, not including the pretransitional thermal effect, amounts to $3.7 \text{ J mol}^{-1} \text{ K}^{-1}$ (see Figure 1). This value and the volume change of 2 Å^3 per formula unit, derived from the X-ray dilatometric measurements (Figure 2b), result in $dT_{32}/dp = 0.33 \text{ K MPa}^{-1}$, which is in good agreement with the coefficient determined directly from the high pressure measurements. A similar estimation can be made for the continuous phase transition at T_{21} by applying the well-known Ehrenfest's relation, $dT/dp = T_0 V_0 \Delta\alpha/\Delta C_p$, where V_0 is the crystal volume at the transition temperature T_0 , and $\Delta\alpha$ and ΔC_p are the changes in the volume thermal expansion coefficient and in the specific heat, respectively. Having determined $\Delta\alpha_{21} = 2.6 \times 10^{-5} \text{ K}^{-1}$ and $V_{21}/Z = 763.3 \text{ Å}^3$ from dilatometric measurements and $\Delta C_p(T_{21}) = 50 \text{ J mol}^{-1} \text{ K}^{-1}$ from DSC measurements, the pressure coefficient $dT_{21}/dp = -0.054 \text{ K MPa}^{-1}$ was calculated. This estimation shows a negative pressure effect on the transition temperature T_{21} and a small magnitude of pressure-induced changes in the low-pressure range, exactly as it is observed experimentally.

CONCLUSIONS

The anionic sublattice of $[\text{C}(\text{NH}_2)_3]_5\text{SO}_4(\text{SO}_3-\text{OC}_2\text{H}_5)_2\text{F}$ consists of three types of ions tied to guanidinium cations by a complex system of $\text{N}-\text{H}\cdots\text{O}$ and $\text{N}-\text{H}\cdots\text{F}$ hydrogen bonds. At ambient pressure, the crystal structure is disordered in the high-temperature phases I and II, which destabilizes the H bond network. On lowering the temperature, the jumps of the ethoxy moieties become correlated, but the dipolar couplings have a clearly short-range character. The application of pressure modifies this picture, leading to the pressure-induced crossover from the local-to-long-range polar order. As a result, the ferroelectric phase occurs at elevated pressures above 140 MPa, but it is stable in a narrow pressure range. When pressure is increased above 220 MPa, the crystal undergoes the phase transition, most probably of the reconstructive nature, and the ferroelectric order vanishes.

Thus, it has been demonstrated that hydrostatic pressure opens the possibility for tuning the structural and dielectric properties of the crystal under study. The relatively low pressure range of the observed phenomena is characteristic for the structures, in which the balance between different interactions is delicate and can be easily disturbed at varied thermodynamic conditions. It seems that, in the case of $[\text{C}(\text{NH}_2)_3]_5\text{SO}_4(\text{SO}_3-\text{OC}_2\text{H}_5)_2\text{F}$, the ionic diversity in the anionic sublattice is one of the principal factors, which determine the crystal properties and thermodynamic behavior.

ASSOCIATED CONTENT

S Supporting Information. Crystallographic information files (CIF) for $[\text{C}(\text{NH}_2)_3]_5\text{SO}_4(\text{SO}_3-\text{C}_2\text{H}_5\text{O})_2\text{F}$ at 120, 200, 240, and 298 K. This material is available free of charge via the Internet at <http://pubs.acs.org>.

AUTHOR INFORMATION

Corresponding Author

*E-mail: masza@amu.edu.pl.

ACKNOWLEDGMENT

This study was supported by Polish Ministry of Science and Higher Education, Grant No. N N202 032240.

REFERENCES

- (1) Russell, V. A.; Etter, M. C.; Ward, M. D. *J. Am. Chem. Soc.* **1994**, *116*, 1941–1952.
- (2) Russell, V. A.; Evans, C. C.; Li, W.; Ward, M. D. *Science* **1997**, *276*, 575–579.
- (3) Swift, J. A.; Pivovar, A. M.; Reynolds, A. M.; Ward, M. D. *J. Am. Chem. Soc.* **1998**, *120*, 5887–5894.
- (4) Mathevet, F.; Masson, P.; Nicoud, J.-F.; Skoulios, A. *Chem.—Eur. J.* **2002**, *8*, 2248–2254.
- (5) Martin, S. M.; Yonezawa, J.; Horner, M. J.; Macosko, C. W.; Ward, M. D. *Chem. Mater.* **2004**, *16*, 3045–3055.
- (6) Mathevet, F.; Masson, P.; Nicoud, J.-F.; Skoulios, A. *J. Am. Chem. Soc.* **2005**, *127*, 9053–9061.
- (7) Holden, A. N.; Matthias, B. T.; Merz, W. J.; Remeika, J. P. *Phys. Rev.* **1955**, *98*, 546.
- (8) Jona, F.; Shirane, G. *Ferroelectric Crystals*; Dover Publications Inc.: New York, 1993.
- (9) Szafranski, M. *Phys. Rev. B* **2005**, *72*, 054122-1–054122-11.
- (10) Szafranski, M.; Katrusiak, A. *Phys. Rev. B* **2006**, *73*, 134111-1–134111-8.
- (11) Szafranski, M. *J. Phys. Chem. B* **2011**, *115*, 8755–8762.
- (12) Szafranski, M.; Jarek, M. *J. Phys. Chem. B* **2008**, *112*, 3101–3109.
- (13) Scott, J. F. *Ferroelectric Memories*; Springer: Berlin-Heidelberg, 2000.
- (14) Uchino, K. *Piezoelectric Actuators and Ultrasonic Motors*; Kluwer Academic: Boston, 1996.
- (15) Gesi, K. *Ferroelectrics* **1986**, *66*, 269–286.
- (16) Gesi, K. *Phase Transitions* **1992**, *40*, 187–215.
- (17) Samara, G. A. *J. Phys.: Condens. Matter* **2003**, *15*, R367–R411.
- (18) Sawada, A.; Kikugawa, T.; Ishibashi, Y. *J. Phys. Soc. Jpn.* **1979**, *46*, 871–875.
- (19) Shimizu, H.; Abe, N.; Kokubo, N.; Yasuda, N.; Fujimoto, S.; Yamaguchi, T.; Sawada, S. *Solid State Commun.* **1980**, *34*, 363–368.
- (20) Gesi, K. *J. Phys. Soc. Jpn.* **1996**, *65*, 1963–1966.
- (21) Diamant, H.; Drenck, K.; Pepinsky, R. *Rev. Sci. Instrum.* **1957**, *22*, 30–33.
- (22) Sheldrick, G. M. Program for Solution of Crystal Structures. SHELXS97; University of Göttingen: Göttingen, Germany, 1997.
- (23) Sheldrick, G. M., Program for Crystal Structure Refinement. SHELXL97; University of Göttingen: Göttingen, Germany, 1997.
- (24) Gómez Cuevas, A.; Pérez Mato, J. M.; Tello, M. J.; Madariaga, G.; Fernández, J.; Echarri, L.; Zuñiga, F. J.; Chapuis, G. *Phys. Rev. B* **1984**, *29*, 2655–2663.